Spontaneous Radiative Cooling to Enhance the Operational Stability of Perovskite Solar Cells via a Black-body-like Full Carbon Electrode

Bingcheng Yu
Institute of Physics
Jiangjian Shi
Institute of Physics
Yiming Li
Institute of Physics
Shan Tan
Institute of Physics
Yuqi Cui
Institute of Physics
Fanqi Meng
Tsinghua University
Huijue Wu
Institute of Physics
Yanhong Luo
Institute of Physics
Dongmei Li
Institute of Physics
Qingbo Meng (qbmeng@iphy.ac.cn)
Institute of Physics

Article

Keywords:

Posted Date: August 11th, 2022

DOI: https://doi.org/10.21203/rs.3.rs-1883905/v1

Abstract

Operational stability of perovskite solar cells is remarkably influenced by the device temperature, therefore, decreasing the interior temperature of the device is one of the most effective approaches to prolong the service life. Herein, we introduce the spontaneous radiative cooling effect into the perovskite solar cell and amplify this effect via functional structure design of a full-carbon electrode (F-CE). Firstly, by the aid of interfacial engineering, >19% and >23% power conversion efficiencies of F-CE based inorganic $CsPbI_3$ and hybrid perovskite solar cells have been achieved, respectively, both of which are the highest reported efficiencies based on carbon electrode and are comparative to the results for metal electrodes. Highly efficient thermal radiation of this F-CE can reduce the temperature of the operating cell by about 10°C. Compared with the conventional metal electrode-based control cells, the operational stability of the above two types of cells have been significantly improved due to this cooling effect. Especially, the $CsPbI_3$ PSCs exhibited no efficiency degradation after 2000 hours continuous operational tracking.

One-Sentence Summary: Thermal radiative cooling effect of full-carbon electrode enhances operational stability of the perovskite solar cells.

Full Text

Solar cells are sensitive to the temperature, and the temperature enhancement will result in performance degradation[1-6]. The elevated temperature of an operating cell mainly comes from the non-photoelectric conversion of the absorbed solar energy[7]. For a cell with a power conversion efficiency (PCE) of 25%, the maximum heating power under 1 sun AM 1.5 G illumination could reach 750 W m^{-2}. Typically for some extreme conditions, this heating power can make the cell temperature exceeding 100°C[8-9]. This high temperature is a severe threat to the cell operational stability, and also put forward higher demand to the encapsulation reliability[10]. Among solar cells, perovskite solar cells (PSCs) are much more sensitive to the elevated temperature[11-16]. Firstly, elevated temperature could cause the organic component volatilization of perovskite absorber materials[11,12], accelerate ion (defect) migration and phase segregation[13,14], and induce metastable crystal structure[15,16]. Secondly, elevated temperature could change or destroy the microstructures of functional layers, even charge transporting ability of the organic hole transporting material[17,18]. Thirdly, elevated temperature could induce and accelerate the atom or component diffusion between different functional layers[19,20].

Numerous works have been reported to overcome this operational stability issue based on improving the heat resistance of functional layers of the cell. For instance, dimension regulation, additive engineering, surface passivation, and process optimization routes are employed to suppress the decomposition or phase transition of perovskite absorber layers at high temperatures[21-24]. A series of new hole transport

layer materials with higher thermal stability have also been developed[25,26]. Although obvious progress has been achieved in the past few years, the stability performance of the PSC is still less satisfactory than commercialized inorganic solar cells.

Along with focusing on materials and interfacial stabilities, thermal management toward the complete cell started to receive attention. The primary concept of thermal management has been introduced to the PSC solar system by reducing the heating power and enhancing the heat dissipation, for example, doping higher thermal conductivity materials, optimizing device geometrical structure, and attaching heat spreaders etc.[27-29]. Under thermal equilibrium conditions, compared to improving interior thermal conduction, enhancing the heat dissipation of the cell terminals actually plays a more critical role in cooling the whole cell. In some practical applications, passive liquid flow cooling or heat sink structures have been integrated into the photovoltaic systems for this purpose; however, these external cooling components would significantly increase the photovoltaic installation and maintenance cost[30-32]. Thus, it is still a challenge to actively cool the operating cell in a low-cost, easy scale-up and large-scale way.

Herein, we introduce the spontaneous radiative cooling effect into the PSC to enhance terminal heat dissipation of the cell. This effect is realized by functional structure design of a full-carbon electrode (F-CE) that simultaneously has high thermal emissivity and excellent electrical properties. Superior interfacial contact and charge transporting ability of the F-CEs contribute to >19% and >23% PCEs of inorganic $CsPbI_3$ and hybrid PSCs, respectively, both of which are the highest reported efficiencies, comparative to the results for metal electrodes. The radiative cooling effect of the F-CEs can reduce the temperature of the operating cell (AM 1.5 G, 1 sun) by ~10°C. For operational stability test, no PCE degradation was found in F-CE based $CsPbI_3$ cell under continuously tracking over 2000 hours. For low/high temperature-cycling test (-20/60 °C), the F-CE based $CsPbI_3$ cell can sustain 95% of the initial PCE over 100 cycles whereas the relative PCE of the Au electrode-based cell drops by >35%. These results suggest that thermal radiative cooling approach of the F-CE electrode can provide a universal, convenient and low-cost solution to overcome the efficiency degradation of the cell induced by temperature elevation during the cell operation.

Heat generation and dissipation properties of PSCs

We first demonstrate the heat generation and dissipation properties of the PSCs. As shown in Fig. 1a, thermal conduction, convection and radiation are the three main heat dissipation pathways. Heat generation properties caused by the light absorption of the PSC are experimentally estimated from light reflection/transmission and external quantum efficiency spectra of the cell (Supplementary Figs. 1-2). It is estimated that the cell absorbs ~97% of the entire sun illumination by the perovskite absorber layer (46%) and other functional layers (51%) (see Fig. 1b). Considering 20% PCE, the heating power of the cell illuminated under AM 1.5G (1 sun) is 770 W m^{-2}. Using these parameters, the cell interior temperature is simulated while considering various thermal radiation configurations (Supplementary Figs. 3-6 and Supplementary Table 1). As presented in Fig. 1c, at room temperature, the interior temperature can reach 94.8°C if the cell does not have thermal radiative cooling. If the cell emits thermal radiation from a single

surface, for example, the conductive glass surface, the temperature obviously decreases to 65.9°C. This could be the practical condition of a PSC with metal back electrode. If the back electrode also emits thermal radiation, the cell temperature will further decrease to 54.5°C, which can guarantee the cell working under a relatively moderate condition. This cooling effect of the dual-face thermal radiation will always work whatever the ambient temperature is. When the cell works in the vacuum, for example, in the near space, this cell cooling effect benefiting from the dual-face thermal radiation will be more impressive (Supplementary Figs. 7).

Inspired by the simulation results, we have designed a triple-layer full-carbon back electrode (F-CE) to realize dual-face thermal radiative cooling for PSCs, as schematically shown in Fig. 1d and Supplementary Figs. 8. This F-CE is comprised of a mesoporous layer having excellent contact with the hole transporting layer (HTL), a highly conductive graphite layer and a thermally radiative layer with efficient thermal radiation ability. Thermal radiative properties of varied electrodes are characterized by IR apparent temperature T_{IR} (measured with IR camera) and their real surface temperature T_0 (measured by thermocouple). When the T_0 increases to 90°C, T_{IR} of the Au electrode is 38.7°C (Fig. 1e). For another alternative electrode, Sn: In_2O_3 (i.e., ITO), its T_{IR} is 48.6°C. Comparatively, T_{IR} of our triple-layer F-CE reaches 89.5°C, very close to the T_0. If the F-CE does not have the thermal radiative layer, its T_{IR} is 66.4°C. Thermal radiation ability of these electrodes is further quantified by using emissivity (ε) [33], that is, $\varepsilon \approx (T_{IR}/T_0)^4$. The ε of the Au and ITO electrode are only 0.034 and 0.085 (Fig. 1f), respectively, and for the simplest single-layer carbon electrode, its ε is 0.93. If a graphite layer is introduced to enhance the carbon electrode conductance, the ε decreases to 0.3 (Fig. 1f and Supplementary Figs. 8). For our designed triple-layer F-CE, the ε reaches 0.98, very close to an ideal black body. In addition, the triple-layer F-CE has large charge conductance because of the interior graphite layer, which is suitable for the PSCs (Supplementary Figs. 9).

Photovoltaic performance of PSCs

We use the F-CE to fabricate inorganic $CsPbI_3$ and hybrid ($FA_{0.97}Cs_{0.03}PbI_{0.97}Br_{0.03}$) PSCs. The cell structure of the $CsPbI_3$ solar cell, comprising of FTO (F: SnO_2) glass, TiO_2, $CsPbI_3$, spiro-OMeTAD and F-CE, is shown in Fig. 2a. Carbon quantum dots (CQD) are introduced to improve the energy alignment of the F-CE/HTL interface. The CQDs are synthesized from hydrothermal method and evenly dispersed in water (Fig. 2b and Supplementary Figs. 10-11). These CQDs with the size of ~ 10 nm, can fill into the undulating area of the F-CE to reduce the surface roughness and modify the work function as well (Supplementary Figs. 12-14). The F-CE is thermally pressed onto the top of the cell, which can guarantee the F-CE robustly contacted with the HTL with adhesive force reaching 3.6 N cm^{-2}, about two orders of magnitude higher than that of the HTL/Au contact (0.07 N cm^{-2}) (Supplementary Figs. 15). This is mainly attributed to the thermal-press approach can make the CE and HTL embed into each other, which will obviously change the film surface morphology and electrical potential (Fig. 2c and d). This not only benefits for the charge interface transfer but also facilitates the heat conduction within the cell.

With the designed F-CE, a record 19.68% PCE (steady-state PCE: 19.23%) has been achieved for the $CsPbI_3$ cell with short-circuit current density (J_{SC}) of 20.36 mA cm^{-2}, open-circuit voltage (V_{OC}) of 1.170 V and fill factor (FF) of 0.826 (Fig. 2e, Supplementary Figs. 16-20, and Supplementary Table 2). In addition, a certified PCE of 19.6% (reverse scanning) is also obtained, comparable to the corresponding Au electrode-based cell (PCE: 20.39%) (Supplementary Figs. 21). In the past few years, PCEs of the carbon-based inorganic perovskite cells (including $CsPbI_3$, $CsPbI_2Br$, $CsPbIBr_2$ and $CsPbBr_3$) indeed rises linearly (Fig. 2f, Supplementary Table 3). As in mid-2021, the highest reported PCE was ~15% while the PCE gap between the Au and carbon-based devices has exceeded 5% in absolute value. Our current result has already narrowed the PCE gap to <1.0%. Besides the $CsPbI_3$ cells, the state-of-the-art carbon-based hybrid PSCs have also been achieved with 23.5% PCE (Supplementary Figs. 22-24). These results demonstrate that the F-CE is a promising electrode technology for the PSCs.

Phase stability of $CsPbI_3$

We further experimentally evaluate the cooling effect of the F-CE on the temperature of the operating cell under AM 1.5 G illumination (Fig. 3a-b). It is found that, the F-CE can reduce the cell surface temperature by ~10°C, from 53.1 (Au electrode) to 45.2 °C; under 2 sun illumination, the cell temperature will reduce from 73.6 to 62.7 °C (Supplementary Figs. 25). This cooling effect will significantly enhance the ambient phase stability of the $CsPbI_3$ film in the cell. As indicated by time-dependent X-ray diffraction (XRD) shown in Fig. 3c-d, β-phase $CsPbI_3$ in the Au based PSC gradually transforms into δ-phase after being illuminated for several hours in ambient conditions. Comparatively, the $CsPbI_3$ in the F-CE based PSC exhibits stable β-phase and constant XRD intensity in the whole illumination aging duration. It is also demonstrated that the temperature itself has obvious influence on the shelf life of the cell. Elevated temperature (such as 65°C) can easily cause PCE degradation and $CsPbI_3$ phase transition in a complete cell, whereas only 10°C reduction will effectively improve the device stability (Supplementary Figs. 26-27).

Stability performance of PSCs

Lastly, we used different aging processes to evaluate the operational stability of the cells. After working at the maximum power point (MPP) under AM 1.5 G (1 sun) for 3000 s in ambient conditions, no PCE degradation can be found for the F-CE based unencapsulated cell, whereas the PCE of the Au-based cell dropped to 92% of its initial value (Fig. 4a). Under concentrated 10 suns illumination, the PCE of the F-CE based cell only decreased to 94% of its initial value, whereas the PCE of the Au electrode-based cell obviously dropped to 78% (Fig. 4b, and Supplementary Figs. 28-29). We further tracked 2000 hour's operational stability in N_2 atmosphere while keeping the cell continuously working under a steady-state bias voltage (0.95 V) and white LED illumination (initial cell current density 20 mA cm^{-2}). The PCE of the F-CE based cell slightly increased in the first 400 hours, then kept almost constant from 500 to 2000 hours (Fig. 4c). To the best of our knowledge, this is one of the best operational stability results among the $CsPbI_3$ solar cells reported so far (Supplementary Table 4). Instead, the PCE of the Au based cell

continuously degraded in the whole aging process, only sustaining 82% of its initial PCE after 2000 hours. Finally, we conducted low-high temperature (-20/60°C) aging test (Fig. 4d). The temperature range between -20 and 60°C was cycled for 100 times by using a semiconductor cooling plate, and the time duration at each temperature in one cycle is 15 min. After the aging process, the PCE of the Au-based cell dropped to <70% of its initial value while the F-CE based cell still can sustain 95% of its initial value. This better temperature-cycling stability mainly benefits from both the temperature buffering effect of the F-CE and the robust HTL/F-CE interface contact (Supplementary Figs. 30).

Conclusions

In this work, we have developed a thermal radiative cooling approach to enhance terminal heat dissipation of the PSC. This effect is realized by the spontaneous radiative cooling effect of a three-layer full-carbon electrode (F-CE), which simultaneously has high thermal emissivity and excellent electrical properties. On the one hand, the superior interfacial contact and charge transporting ability of the F-CEs contribute to > 19% and > 23% PCEs of inorganic $CsPbI_3$ and hybrid PSCs, respectively, both of which are the highest reported efficiencies based on carbon electrode, comparable to PCEs for metal electrodes. Besides, highly efficient thermal radiation of this F-CE can reduce the temperature of the operating cell by about 10°C. This F-CE based cell exhibits excellent operational stability with almost no efficiency degradation after 2000 hours of continuous operational tracking. Our work provides a robust solution to enhancing the operational stability of PSCs based on the F-CEs by the aid of thermal radiative cooling effect, which thus will facilitate the commercialization of PSCs.

Methods

Materials. Lead (II) iodide (PbI_2, 99.9985%), SnO_2 colloidal dispersion (tin (IV) oxide, 15% in H_2O colloidal dispersion) and chlorobenzene (CB, 99.9%) were purchased from Alfa Aesar. Formamidinium iodide (FAI, 99.5%) formamidinium bromide (FABr, 99.5%) and methylammonium chloride (MACl, 99.5%) were purchased by Xi'an Polymer Light Technology Corp. Cesium iodide (CsI, 99.9%) were purchased from Sigma-Aldrich. Hydroidic acid (HI, 55.0–58.0%), Trimethylphenylammonium iodide (TPAI, 99%) was purchased from Aladdin. The N, N-Dimethylformamide (DMF), dimethyl sulfoxide (DMSO), chlorobenzene (CB), and 4-tert-butylpyridine (TBP, 99.999%) were purchased from Alfa Aesar. Spiro-OMeTAD was purchased from Luminescence Technology Corp. (Lumtec). bis(trifluoromethane)sulfonimide lithium salt (LiTFSI) was from Sigma-Aldrich (99.9985%), tris(2-(1H-pyrazol-1-yl)-4-tert-butylpyridine)-cobalt (III)tris(bis(trifluoromethylsulfonyl)imide) (FK209 Co (III) TFSI) were from Dyesol. Unless stated otherwise, solvents and chemicals were obtained commercially and were used without further purification. The $DMAPbI_3$ and conductive carbon paste was homemade using the methods reported by the previous literatures [34, 35].

Precursor solution preparation. (1) Electron transport layer (ETL) solution: The TiO_2 sol-gel precursors solution was prepared by dissolving 0.125 M titanium isopropoxide and 0.125 M HCl in *n*-butylalcohol.

(2) Inorganic perovskite solution: The perovskite precursor solution was prepared by dissolving 462.7 mg $DMAPbI_3$, 189.6 mg CsI and 0.3 mg thiocyanate molten salt in 1 ml of DMF/DMSO mixed solvent (v: v = 8.5: 1.5), more details can be seen in our previous work [34]. The precursor solution was stirred for 5 hours at room temperature and was filtered before use. (3) Organic-inorganic hybrid perovskite solution: The perovskite precursor solution was prepared by dissolving 800.3 mg PbI_2, 275.2 mg FAI, 6.0 mg FABr, 12.5 mg CsI and 34.9 mg MACl in 1 ml of DMF/DMSO mixed solvent (v: v = 8.5: 1.5). The precursor solution was stirred for 5 hours at room temperature and was filtered before use. (4) Hole transport layer (HTL) solution: The spiro-OMeTAD solution was prepared by dissolving spiro-OMeTAD in CB (60 mM) with the additives of Li-TFSI, FK209 and TBP at doping molar ratios of 0.5, 0.03 and 3.3.

Carbon quantum dots (CQDs) synthesis. CQDs were prepared as follows, citric acid (1.0507 g) and ethylenediamine (335 μL) was dissolved in DI-water (10 mL). Then the solution was transferred to a poly(tetrafluoroethylene) (Teflon)-lined autoclave (30 mL) and heated at 200 ℃ for 5 h. After the reaction, the reactors were cooled to room temperature by naturally. The product, which was brown-black and transparent, was subjected to dialysis in order to obtained the CQDs.

Carbon electrode (CE) fabrication. Firstly, the lab-made conductive-carbon paste was coated on carbon graphite paper substrate by doctor-blading, forming wet carbon films. Then, the carbon films were soaked into ethanol for 10 min at room temperature to remove residual solvent, obtaining C1 films. In order to obtain a carbon film modified with CDs (C2 films), C1 is continuously soaked in an aqueous solution of carbon quantum dots for 2 minutes. Furthermore, in order to obtain the full-carbon electrode (F-CE), a carbon film can be scraped on the back of the carbon graphite paper corresponding to the C1 and C2 carbon films for heat radiation heat dissipation.

Solar cell fabrication. (1) FTO substrates preparation: Laser-patterned FTO glass (sheet resistance of 8.5 $\Omega\ sq^{-1}$) was sequentially cleaned with a mild detergent, alkali liquor, distilled water, and ethanol in an ultrasonic bath. The substrate was treated with ozone for 30 min prior to use. The size of the substrate for preparing small-area (0.09 cm^{-1}) cells is 1.5 × 1.5 cm^2. The size of the substrate for preparing large-area (1.0 cm^{-1}) cells is 2.0 × 3.0 cm^2. (2) ETL fabrication: The compact TiO_2 layer was deposited on the FTO glass with a 0.125 M titanium (IV) isopropoxide sol-gel precursor solution by spin coating at 3000 rpm (with a ramping rate of 2000 rpm s^{-1}), and then the samples were sintered at 500℃ for 1 h. To further improve the electron transport capability, the compact TiO_2 layer was treated with 0.025 M $TiCl_4$ aqueous solution for 30 min, and then the samples were sintered at 500℃ for 1 h. For the ETL used in organic-inorganic perovskite solar cells (PSCs), a thin SnO_2 layer needs to be spin coated onto the pre-cleaned TiO_2 substrate using a SnO_2 colloidal dispersion solution in water (1.50%) at 5000 rpm for 30 s and annealed at 150°C for 30 min in ambient atmosphere. (3) Inorganic perovskite films: Perovskite films were fabricated by two-step annealing method. In details, the $CsPbI_3$ active layer was spin-coated on 50°C pre-warmed TiO_2/FTO substrate (1500 rpm for 10 s with a ramping rate of 500 rpm s^{-1} and subsequently at 4000 rpm for 30 s with a ramping rate of 1500 rpm s^{-1}). spin-coated at. After spin-coated, the precursor films were firstly placed onto the hotplate with 70°C for about 3 min (depends on the color of

the film) to afford the transition film. Subsequently, the substrates were placed onto the hotplate with 200°C for 10 min in dry air (~ 15% RH) to evaporate the solvents and further enhance the crystallization of perovskites. (4) Organic-inorganic perovskite films: Perovskite films were fabricated by anti-solvent single-step spin-coating method. In details, the perovskite precursor solution was spin-coated at 1000 rpm for 10 s with a ramping rate of 500 rpm s^{-1} and subsequently at 5000 rpm for 30 s with a ramping rate of 1500 rpm s^{-1}, CB (120 μL) was poured onto the substrate at 15 s during the high-speed stage. The half-crystallization film was heated at 150°C for 10 min in dry air (RH: 20 ~ 30%). After cooling down, 1.3 mg/mL of TPAI in chloroform was spin-coated at 3000 rpm to passivate the surface of perovskite films. (5) HTL films: To make a HTL based on spiro-OMeTAD, 20 μl of spiro-OMeTAD (60 mM) was spin-coated on the top of perovskite layer at the speed of 3000 rpm (with a ramping rate of 2000 rpm s^{-1}) for 30 s in a N_2-filled glovebox. The films were heated at 60 ℃ for 8 min. (6) Electrode fabrication: For Au electrode-based devices, Au electrode about 80 nm was deposited via thermal evaporation under the vacuum of 10 − 7 Torr. For carbon electrode-based devices, two kinds of carbon films were directly pressed onto spiro-OMeTAD layer under a pressure of 0.7 MPa, more details can be seen in our previous work.

Characterization. UV-Vis transmission and reflection properties (200–3000 nm) was recorded on a spectrophotometer (UV-3600plus, Shimadzu, Japan). The background noise was subtracted before testing. XRD patterns were performed by using 40 kV, 40 mA Cu Kα (λ = 0.15406 nm) radiation by Mini Flex 600 (Rigaku, Japan). Surface morphologies of carbon films and complete device were studied by scanning electron microscopy (SEM, Sigma 300, Zeiss, Germany). The transmission-electron microscopy (TEM) images were obtained on JEM-F200CF (JEOL). The Atomic force microscopy (AFM) and Kelvin probe force microscopy (KPFM) measurements were carried out on atomic force microscope (Multimode 9, Bruker, Germany) at room temperature and in the dark. The Tapping mode AFM (TM-AFM) and KPFM (TM-KPFM) were used to probe top-view surface morphologies and surface potential, respectively. Infrared imaging measurements were carried out at room temperature (~ 25°C) by using a FLIR thermal infrared camera (FLIR ONE Pro, FLIR, USA). Optical images of samples were measured on metallographic microscope (OLYMPUS, BX61). The CQDs for Fourier transform infrared (FT-IR) characterization were dispersed in deionized water. FT-IR spectra were performed on TENSOR 27 spectrometer. The Current density-voltage (*J-V*) characteristics were measured with Keithley 2602 source meter with a scan rate of 50 mV s^{-1} under AM 1.5G (100 mW cm^{-2}) irradiance from solar simulated (Zolix SS150A). The light intensity of 100 mW cm^{-2} was calibrated by using a standard silicon solar cell. The solar cells were masked with a black mask to define the active area of 0.09 cm^2 and 1.0 cm^2, respectively. *J-V* measurements of non-encapsulated solar cells were performed at ambient condition, the scanning speed was 50 mV s^{-1} with a delay time of 0.3 s. The External quantum efficiency (EQE) of non-encapsulated solar cells were measured in air on Enli Technology (Taiwan) EQE system. A standard-monocrystalline silicon cell was used as the reference for EQE tests. No pre-light soaking and pre-bias were applied over the measurement time. The Adhesion between different electrodes and HTL tested by tape-tear method. The strength of the adhesion can be reflected by the peak reading of the tension meter (HANDPI, HP-100)

Stability test. The stability studies involved in this work were all on unencapsulated devices. The devices operating the normal and concentrated AM 1.5 illumination in ambient condition, respectively. The devices were constantly cooled by blasting air stream onto the devices (FTO side) with the device surface measuring approximately 25°C. The long-term operation stability of the devices was tested under continuous white LED illumination in N_2 atmosphere and constant bias voltage applied. The devices for thermal cycle stability were placed on a temperature control platform in N_2 glove box, and a certain program is used to perform high and low temperature cycles.

Heat-Transfer simulations. Finite-element (FEM) heat transfer simulations were performed using COMSOL Multiphysics (COMSOL, Inc.). The Glass, perovskite, spiro-OMeTAD and Au electrode with the dimensions of 0.5×0.5×2.0 mm^3, 0.5×0.5×0.0005 mm^3, 0.5×0.5×0.0002 mm^3, and 0.5×0.5×0.00008 mm^3 was modeled, respectively. The initial temperature was set to 25℃ in the entire model. No temperature boundary conditions were applied. To simplify the model, we equivalent the perovskite absorption layer under 1 Suns with heat fluxes of $7.0×10^8$ W m^3. The heat transfer analysis required specification of thermal conductivity, specific heat density in this study which are listed in Supplementary Table 1.

References

1. Tress, W. et al. Performance of perovskite solar cells under simulated temperature-illumination real-world operating conditions. Nat. Energy **4**, 568-574 (2019).
2. Tress, W. et al. Interpretation and evolution of open-circuit voltage, recombination, ideality factor and subgap defect states during reversible light-soaking and irreversible degradation of perovskite solar cells Energy Environ. Sci. **11**, 151-165 (2018).
3. Haschke, J. et al. The impact of silicon solar cell architecture and cell interconnection on energy yield in hot & sunny climates. Energy Environ. Sci. **10**, 1196-1206 (2017).
4. Kersten, F. et al. Degradation of multicrystalline silicon solar cells and modules after illumination at elevated temperature. Sol. Energy Mater Sol. Cells **142**, 83-86 (2015).
5. Zuschlag, A. Skorka, D. & Hahn, G. Degradation and regeneration in mc-Si after different gettering steps. Prog. Photovolt. **25**, 545-552 (2017).
6. Singh, P. & Ravindra, N. M. Temperature dependence of solar cell performance-an analysis. Sol. Energy Mater Sol. Cells **101**, 36-45 (2012).
7. Xu, L. et al. Heat generation and mitigation in silicon solar cells and modules. Joule **5**, 631-645 (2021).
8. Tu, Y. et al. Perovskite Solar Cells for Space Applications: Progress and Challenges. Adv. Mater. **33**, e2006545 (2021).
9. Thirsk, R. Kuipers, A. Mukai, C. & Williams, D. The space-flight environment: the International Space Station and beyond. Can. Med. Assoc. J. **180**, 1216-1220 (2009).
10. de Oliveira, M.C.C. Diniz, A.S.A.C. Viana, M.M. & Lins, V.D.C. The causes and effects of degradation of encapsulant ethylene vinyl acetate copolymer (EVA) in crystalline silicon photovoltaic modules: A

review. Renew. Sust. Energ. Rev. **81**, 2299-2317 (2018).

11. Conings, B. et al., Intrinsic Thermal Instability of Methylammonium Lead Trihalide Perovskite. Adv. Energy Mater. **5**, 1500477 (2015).
12. Juarez-Perez, E.J. Hawash, Z. Raga, S.R. Ono, L.K. & Qi, Y. Thermal degradation of $CH_3NH_3PbI_3$ perovskite into NH_3 and CH_3I gases observed by coupled thermogravimetry–mass spectrometry analysis. Energy Environ. Sci. **9**, 3406-3410 (2016).
13. Yuan, Y. et al. Electric-Field-Driven Reversible Conversion Between Methylammonium Lead Triiodide Perovskites and Lead Iodide at Elevated Temperatures. Adv. Energy Mater. **6**, 1501803 (2016).
14. Knight, A.J. & Herz, L.M. Preventing phase segregation in mixed-halide perovskites: a perspective. Energy Environ. Sci. **13**, 2024-2046 (2020).
15. Steele, J.A. et al. Thermal unequilibrium of strained black $CsPbI_3$ thin films. Science **365**, 679-684 (2019).
16. Chen, S. et al. Atomic scale insights into structure instability and decomposition pathway of methylammonium lead iodide perovskite. Nat. Commun. **9**, 4807 (2018).
17. Jena, A.K. Ikegami, M. & Miyasaka, T. Severe Morphological Deformation of Spiro-OMeTAD in $(CH_3NH_3)PbI_3$ Solar Cells at High Temperature. ACS Energy Lett. **2**, 1760-1761 (2017).
18. Boyd, C.C. Cheacharoen, R. Leijtens, T.& McGehee, M.D. Understanding Degradation Mechanisms and Improving Stability of Perovskite Photovoltaics. Chem. Rev. **119**, 3418-3451 (2019).
19. Wu, S. et al. A chemically inert bismuth interlayer enhances long-term stability of inverted perovskite solar cells. Nat. Commun. **10**, 1161 (2019).
20. Zhao, Y. A bilayer conducting polymer structure for planar perovskite solar cells with over 1,400 hours operational stability at elevated temperatures. Nat. Energy **7**, 144-152 (2021).
21. Liang, C. et al. A bilayer conducting polymer structure for planar perovskite solar cells with over 1,400 hours operational stability at elevated temperatures. Nat. Energy **6**, 38-45 (2020).
22. Turren-Cruz, S.H. Hagfeldt, A. & Saliba, M. Methylammonium-free, high-performance, and stable perovskite solar cells on a planar architecture. Science **362**, 449-453 (2018).
23. Wu, G. et al. Surface Passivation Using 2D Perovskites toward Efficient and Stable Perovskite Solar Cells. Adv. Mater. **34**, e2105635 (2022).
24. Wang, Y. et al. Thermodynamically stabilized b-$CsPbI_3$-based perovskite solar cells with efficiencies >18%. Science **365**, 591–595 (2019).
25. Jeon, N.J. et al. A fluorene-terminated hole-transporting material for highly efficient and stable perovskite solar cells. Nat. Energy **3**, 682-689 (2018).
26. Arora, N. et al. Perovskite solar cells with CuSCN hole extraction layers yield stabilized efficiencies greater than 20%. Science **358**, 768-771(2017).
27. Pei, F. et al. Thermal Management Enables More Efficient and Stable Perovskite Solar Cells. ACS Energy Lett. **6**, 3029-3036 (2021).

28. Yang, N. et al. Improving Heat Transfer Enables Durable Perovskite Solar Cells. Adv. Energy Mater. **12**, 2200869 (2022).
29. Choi, K. et al. Heat dissipation effects on the stability of planar perovskite solar cells. Energy Environ. Sci. **13**, 5059-5067 (2020).
30. Chauhan, A. et al. Futuristic approach for thermal management in solar PV/thermal systems with possible applications. Energ. Convers. **163**, 314-354 (2018).
31. Elavarasan. R.M. Tyagi, V.V. & Anand, S.. Pathways toward high-efficiency solar photovoltaic thermal management for electrical, thermal and combined generation applications: A critical review. Energ. Convers. **255**, 115278 (2022).
32. Browne, M.C. Norton, B. & McCormack, S.J. Phase change materials for photovoltaic thermal management. Renew. Sust. Energ. Rev. **47**, 762-782 (2015).
33. Tang, K. et al. A Thermal Radiation Modulation Platform by Emissivity Engineering with Graded Metal-Insulator Transition. Adv. Mater. **32**, e1907071 (2020).
34. Yu, B. et al. Efficient (>20 %) and Stable All-Inorganic Cesium Lead Triiodide Solar Cell Enabled by Thiocyanate Molten Salts. Angew. Chem. Int. Ed. **60**, 13436-13443 (2021).
35. Zhang, H. et al. Self-Adhesive Macroporous Carbon Electrodes for Efficient and Stable Perovskite Solar Cells. Adv. Funct. Mater. **28**, 1802985(2018).

Declarations

Acknowledgments

This work was supported by the Ministry of Science and Technology of the People's Republic of China (2021YFB3800103) and the National Natural Science Foundation of China (Nos.11874402,51872321,52172260,52072402,52102332,51627803).

Author contributions

D.L. and Q.M. conceived of the work. B.Y. and J.S. fabricated and characterized solar cells. B.Y. and J.S. conducted temperature measurements. B.Y. conducted temperature simulations on the device model under different conditions. B.Y. conducted the synthesis and characterization of the CQDs. Y.L. conducted AFM and KPFM experiments, performed AFM and KPFM analysis. Y.C. conducted SEM experiments, performed SEM analysis, and conducted the XRD measurements. F.M. conducted the TEM measurements. H.W conducted the EQE measurements. B.Y. and Y.L conducted stability tests on the devices.D.L. and Q.M. directed and supervised the project. B.Y. and J.S. wrote the first draft of the paper. D.L. and Q.M. revised the paper. All authors analyzed their data and reviewed and commented on the paper.

Competing interests

Authors declare that they have no competing interests.

Figures

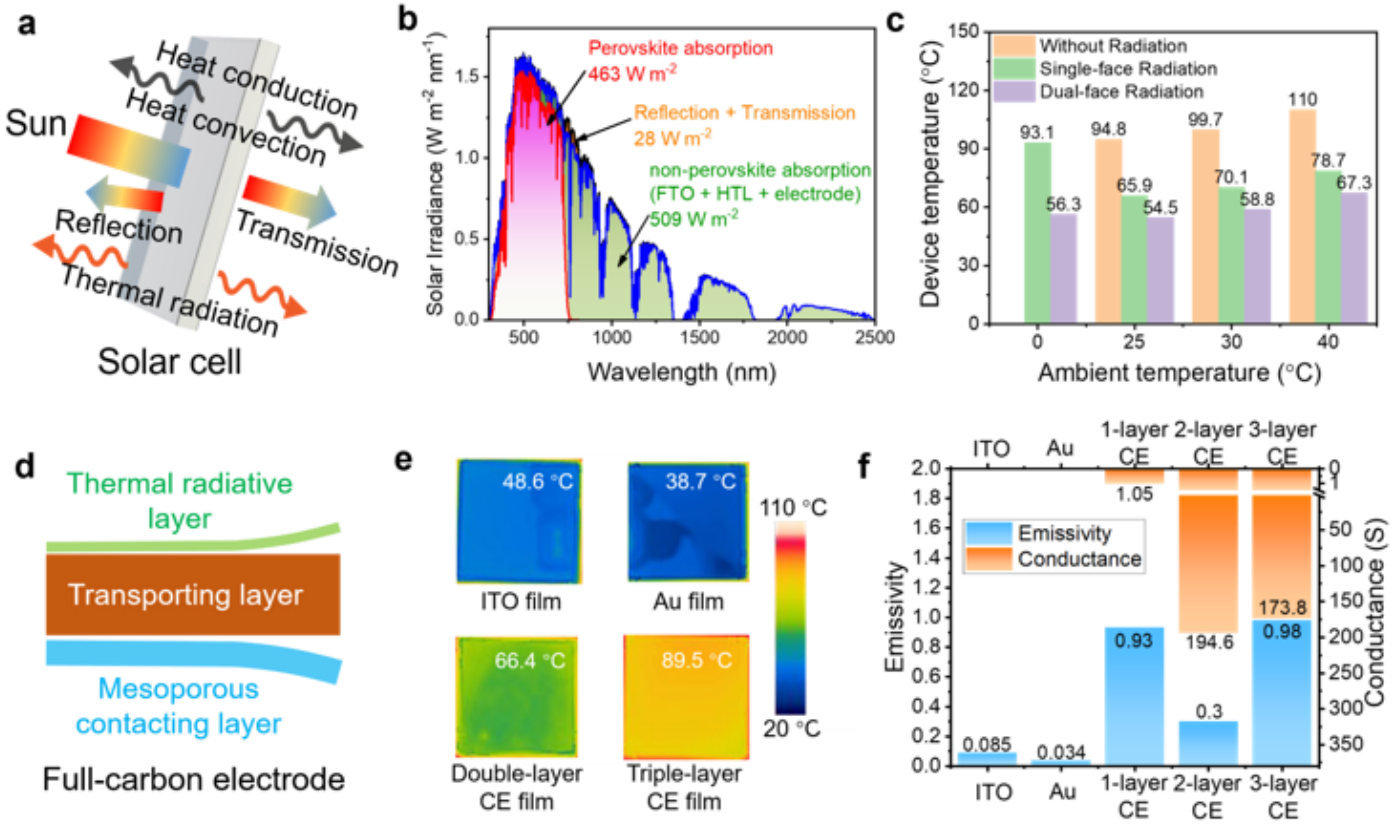

Figure 1

Thermal properties of the PSC and the radiative F-CE. a, Schematic diagram of the sun illumination and heat dissipation pathways of the cell. **b**, Absorption of the AM 1.5 G solar irradiance spectrum by different parts of the cell, estimated from cell external quantum efficiency and reflection/transmission spectra. **c**, Simulated cell temperature under heating power of 770 W m^{-2}. **d**, Schematic diagram of the designed triple-layer F-CE comprising of mesoporous contacting, transporting and thermal radiative layers. **e**, IR camera measured temperature of varied electrodes having surface temperature of about 90 °C. **f**, Emissivity and conductance of the electrodes.

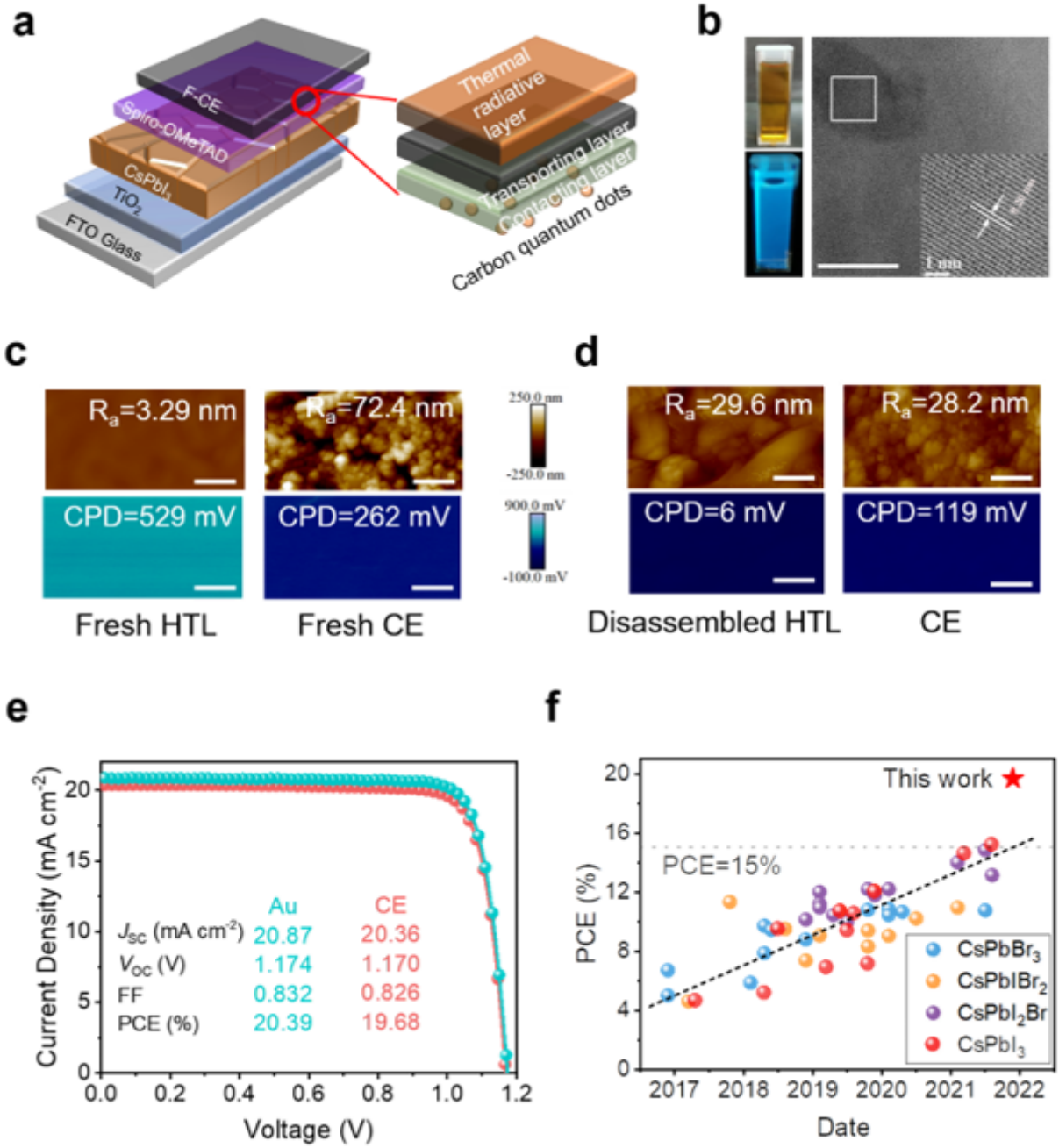

Figure 2

F-CE-based $CsPbI_3$ solar cell. a, Structure of the cell and the F-CE. Carbon quantum dots (CQD) are used to engineer the rear interface (the thermal radiative layer: dense carbon film; transporting layer: graphite paper; contacting layer: porous carbon film). **b**, Photos of the CQD solution and its photoluminescence, and high-resolution transmission electron microscope image of the CQDs. Scale bar: 10 nm. Inset: lattice fringe image. **c**, **d**, Surface morphology and contacting potential difference (CPD) of the fresh HTL and F-CE (**c**) and of them disassembled from the cell (**d**), respectively. Scale bar: 1 μm. **e**, Current-voltage (*I-V*) characteristics of champion cells with Au electrode and F-CE, respectively. **f**, PCE progress of the carbon electrode (CE) based inorganic $CsPb(I, Br)_3$ PSCs.

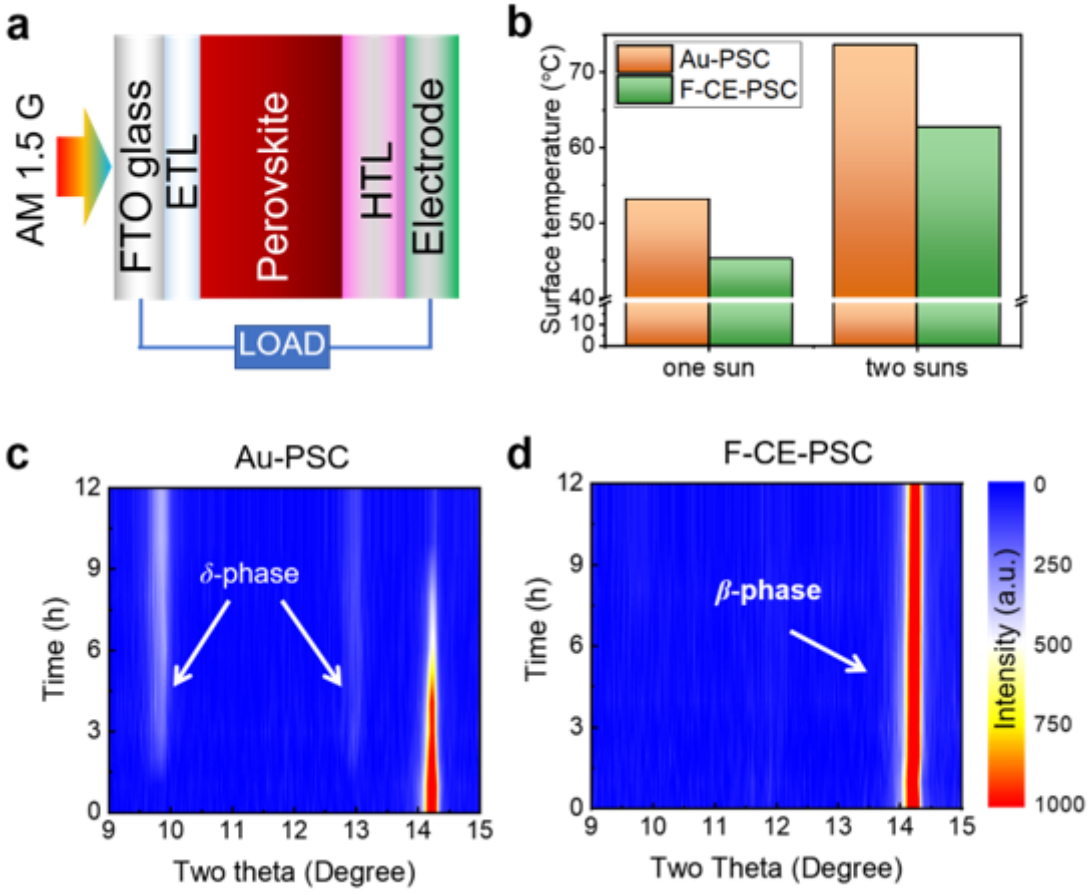

Figure 3

Influence of F-CE on the cell temperature and $CsPbI_3$ phase stability. a, Temperature measurement of an operating PSC under AM 1.5 G illumination. **b**, Influence of electrode on the cell temperature. **c**, **d**, Time-dependent X-ray diffraction patterns of the $CsPbI_3$ in the cells with varied electrodes under continuous light illumination (LED, about 6×10^5 lx).

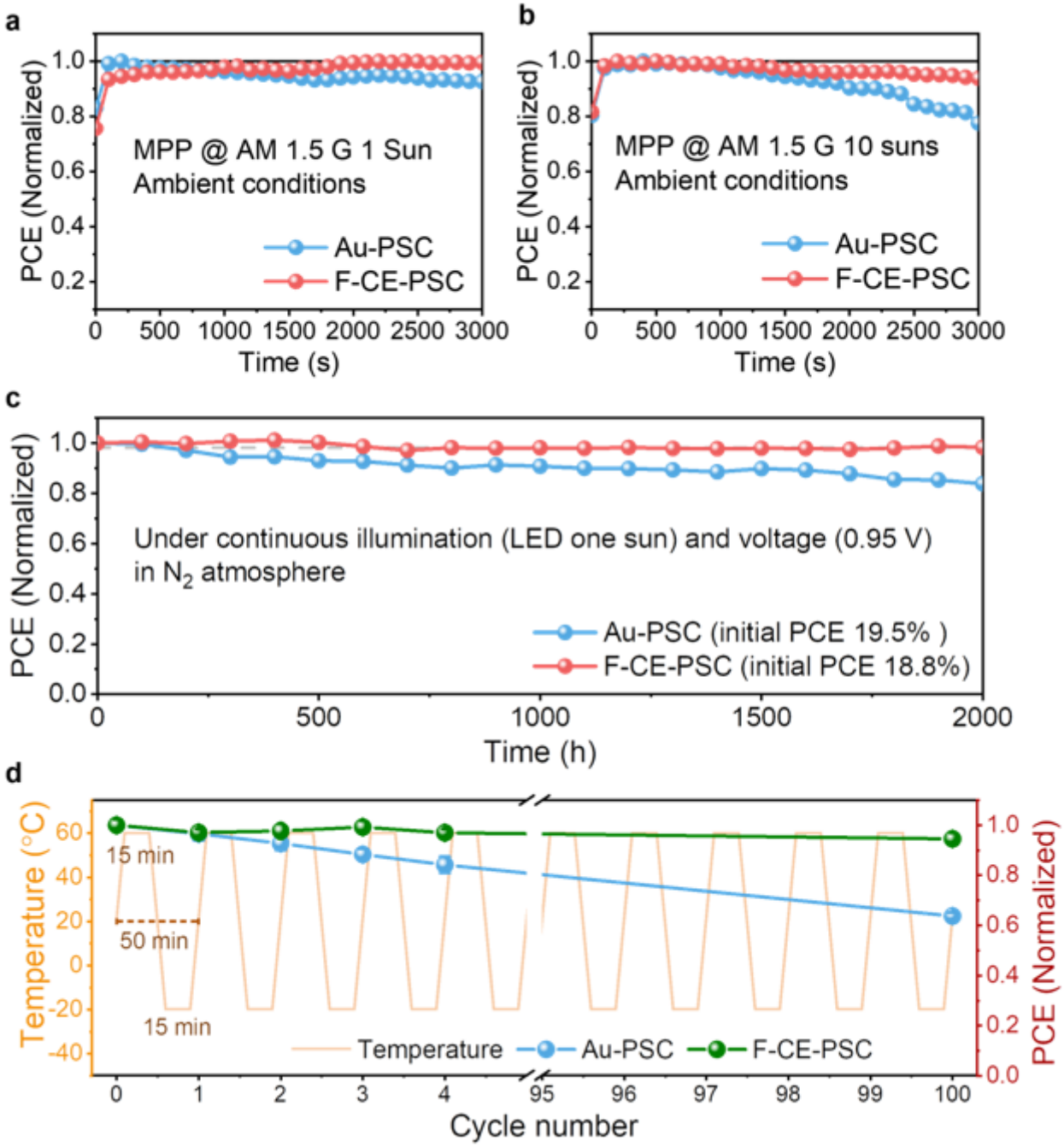

Figure 4

Operational stability test of the cell. a, **b**, PCE tracking of the cells operating under normal and 10× concentrated AM 1.5G illumination in ambient conditions. **c**, 2000 h PCE tracking of the cells continuously operating under light illumination (initial cell current density 20 mA cm^{-2}) and bias voltage (0.95 V) in N_2 atmosphere. **d**, Low (-20°C) -high (60°C) temperature cycling test in N_2 atmosphere for 100 cycles.

Supplementary Files

This is a list of supplementary files associated with this preprint. Click to download.

- SupplementaryMaterialsWord.docx